RESEARCH ARTICLE

Open Access

A chip-based optoelectronic-oscillator frequency comb

Jinbao Long[1†], Zhongkai Wang[1†], Huanfa Peng[2†], Wei Sun[1], Dengke Chen[1,3], Shichang Li[1,3], Shuyi Li[1], Yi-Han Luo[1], Jijun He[4], Lan Gao[1], Baoqi Shi[1], Chen Shen[1,5], Linze Li[6], Tianyu Long[6], Baile Chen[6], Zhenyu Li[7] and Junqiu Liu[1,8*]

Abstract

Microresonator-based Kerr frequency combs ("Kerr microcombs") constitute chip-scale frequency combs of broad spectral bandwidth and repetition rate ranging from gigahertz to terahertz. A critical application that exploits the coherence and high repetition rate of microcombs is microwave and millimeter-wave generation. Latest endeavor applying two-point optical frequency division (OFD) to photonic-chip-based microcombs has created microwaves with remarkably low phase noise. Nevertheless, existing approaches to achieve exceptionally coherent microcombs still require extensive active locking, additional lasers, and external RF or microwave sources, as well as sophisticated initiation. Here we demonstrate a simple and entirely passive (no active locking) architecture, which incorporates an optoelectronic oscillator (OEO) and symphonizes a coherent microcomb and a low-noise microwave spontaneously. Our OEO microcomb leverages state-of-the-art integrated chip devices, including a high-power DFB laser, a broadband silicon Mach–Zehnder modulator, an ultralow-loss silicon nitride microresonator, and a high-speed photodetector. Each can be manufactured in large volume with low cost and high yield using established CMOS and III-V foundries. Our system synergizes a microcomb of 10.7 GHz repetition rate and an X-band microwave with phase noise of − 97/ − 126/ − 130 dBc/Hz at 1/10/100 kHz Fourier frequency offset, yet does not demand active locking, additional lasers, and external RF or microwave sources. With potential to be fully integrated, our OEO microcomb can become an invaluable technology and building block for microwave photonics, radio-over-fiber, and optical communication.

[†]Jinbao Long, Zhongkai Wang and Huanfa Peng have contributed equally to the work.

*Correspondence:
Junqiu Liu
liujq@iqasz.cn
[1] International Quantum Academy, Shenzhen 518048, China
[2] Institute of Photonics and Quantum Electronics (IPQ), Karlsruhe Institute of Technology (KIT), Karlsruhe 76131, Germany
[3] Shenzhen Institute for Quantum Science and Engineering, Southern University of Science and Technology, Shenzhen 518055, China
[4] Key Laboratory of Radar Imaging and Microwave Photonics, Ministry of Education, Nanjing University of Aeronautics and Astronautics, Nanjing 210016, China
[5] Qaleido Photonics, Shenzhen 518048, China
[6] School of Information Science and Technology, ShanghaiTech University, Shanghai 201210, China
[7] Linkstar Microtronics Pte. Ltd, Singapore 118222, Singapore
[8] Hefei National Laboratory, University of Science and Technology of China, Hefei 230088, China

1 Introduction

Optical frequency combs (OFC) [1–3], which coherently channel radio and microwave frequency to the optical domain, have revolutionized timing, spectroscopy, and precision measurement, as well as the fundamental physics test. Conventionally constructed with solid-state or fiber mode-locked lasers, today OFCs can be built on-chip [4–6]. This advancement has been made possible by the emergence and rapid maturation of low-loss photonic integrated circuit based on a variety of material platforms [7–9], along with hybrid and heterogeneous integration [10–12]. Photonic-chip-based OFCs have small size, weight, and power consumption and can be manufactured in large volume with low cost and high yield, ideal for wide deployment outside laboratories and in space.

The most leading type of photonic-chip-based OFCs is established on low-loss, Kerr nonlinear optical micro-resonators driven by continuous-wave (CW) lasers, which is commonly referred to as "Kerr microcombs" [13–26]. Microcombs exhibit broad spectral bandwidths and repetition rates in the gigahertz to terahertz range. One critical application benefiting from the coherence and high repetition rate of microcombs is microwave and millimeter-wave generation [17–21]. Photodetection of the microcomb pulse stream generates a low-noise microwave or millimeter-wave whose carrier frequency corresponds to the microcomb's repetition rate. Various approaches have been demonstrated to improve the microwave's spectral purity, aided by an external micro-wave [19, 27], an auxiliary laser [28], a transfer comb [29], or operation in the "quiet point" [30, 31]. Notably, latest endeavor has applied optical frequency division (OFD) [32–34] on photonic-chip-based microcombs, catalyzing microwaves with superior phase noise performance [35–39]. Nevertheless, microcomb-based OFD still requires extensive active locking, additional lasers, and external RF or microwave sources, as well as sophisticated initiation.

Here we demonstrate a simple and entirely passive architecture that combines an optoelectronic oscillator (OEO) and a Kerr nonlinear microresonator. The system spontaneously generates an exceptionally coherent microcomb whose repetition rate features ultralow RF phase noise. Figure 1a depicts the conceptual diagram of our "OEO microcomb". An OEO comprises hybrid optical and microwave components, forming a photonic microwave oscillator with ultrahigh RF spectral purity [40–44] and without any active feedback phase control. Modern OEOs have achieved unprecedentedly low phase noise, e.g. down to -163 dBc/Hz at 6 kHz offset for 10 GHz carrier [45], surpassing high-end electrical counterparts. Moreover, chip-scale OEOs can be built with photonic integrated circuit based on silicon on insulator (SOI) or indium phosphide (InP) [46].

Figure 1b illustrates the working principle of our OEO microcomb. The CW output from a distributed feedback (DFB) laser is intensity-modulated with a silicon Mach–Zehnder modulator (Si MZM), creating pairs of optical sidebands in the frequency domain. The modulated light is coupled into a high-Q silicon nitride (Si_3N_4) optical microresonator. When the Si MZM's modulation frequency f_{IM} matches the microresonator's free spectral range (FSR, $D_1/2\pi$), i.e. $f_{IM} = D_1/2\pi$, a coherent microcomb forms [47–50]. In the frequency domain, the microcomb contains many mutually coherent CW tones that are equidistantly spaced by $D_1/2\pi$. In the time domain, it is a pulse stream of repetition rate $f_{rep} = D_1/2\pi$. Detection of the microcomb via a photodetector (PD) produces

a fundamental microwave tone with carrier frequency of f_{rep}. Collecting and injecting the microwave back into the Si MZM ensures $f_{IM} = f_{rep} = D_1/2\pi$. As such, the entire system can self-oscillate and self-maintain, harmonizing a coherent microcomb and a low-noise microwave. Figure 1c presents a photograph of the four chip components of our OEO microcomb – a DFB laser chip, a Si MZM chip, a Si_3N_4 microresonator chip, and a PD chip. The chip sizes are referenced with a ruler. Figure 1d and e show the zoomed-in optical microscope images of the III-V-semiconductor-based DFB laser chip and an individual PD on the PD chip. Details on the performance characterization of each chip components are summarized in Fig. 2 and described below.

2 Results

2.1 Characterization of individual chip components

Laser. The commercial DFB laser outputs 83 mW CW power around 1558 nm with 300 mA current and trans-verse-electric (TE) polarization. A printed circuit board (PCB) is used to stabilize the laser current and tem-perature at 25 ℃. Figure 2a shows that the laser exhibits 13 mA current at threshold, and 0.6 nm wavelength tun-ability over 300 mA current range. Figure 2b shows the measured frequency noise of the free-running laser, i.e. single-sideband power spectral density (PSD) of the laser frequency noise. The intrinsic linewidth is calculated as 2.79 kHz from the white noise of 445 Hz^2/Hz. More information on the DFB laser is found in Supplementary Materials Note 1.

Modulator. The Si MZM, fabricated in a standard CMOS foundry, is a traveling-wave (TW) MZM with a push-pull configuration. The design and simulation are found in Ref. [51]. Modulation is achieved via the plasma dispersion effect in depletion-type PN junctions within the two waveguide arms. The Si MZM's microwave-to-optical conversion efficiency is characterized by the product of half-wave voltage V_π and phase-shift length L_π, i.e. $V_\pi L_\pi$, which can be measured by applying a bias voltage V_{dc} to the upper or lower waveguide arm of the MZM. Figure 2c and d show the Si MZM's transmission spectrum with different V_{dc} values applied on the upper (c) or lower arm (d). By calculating the dip shift on the transmission spectrum under varying V_{dc}, the $V_\pi L_\pi$ of our Si MZM is calculated as 2 V · cm. More informa-tion on the Si MZM is found in Supplementary Materi-als Note 2. Based on the eye-diagram measurement and numerical simulation in Supplementary Materials Note 2, the Si MZM's bandwidth is evaluated to be between 20 to 46 GHz. Note that, essentially the microwave feedback signal can be directly applied to modulate the laser. This scenario can save the Si MZM and simplify our system. However, this configuration does not work here because
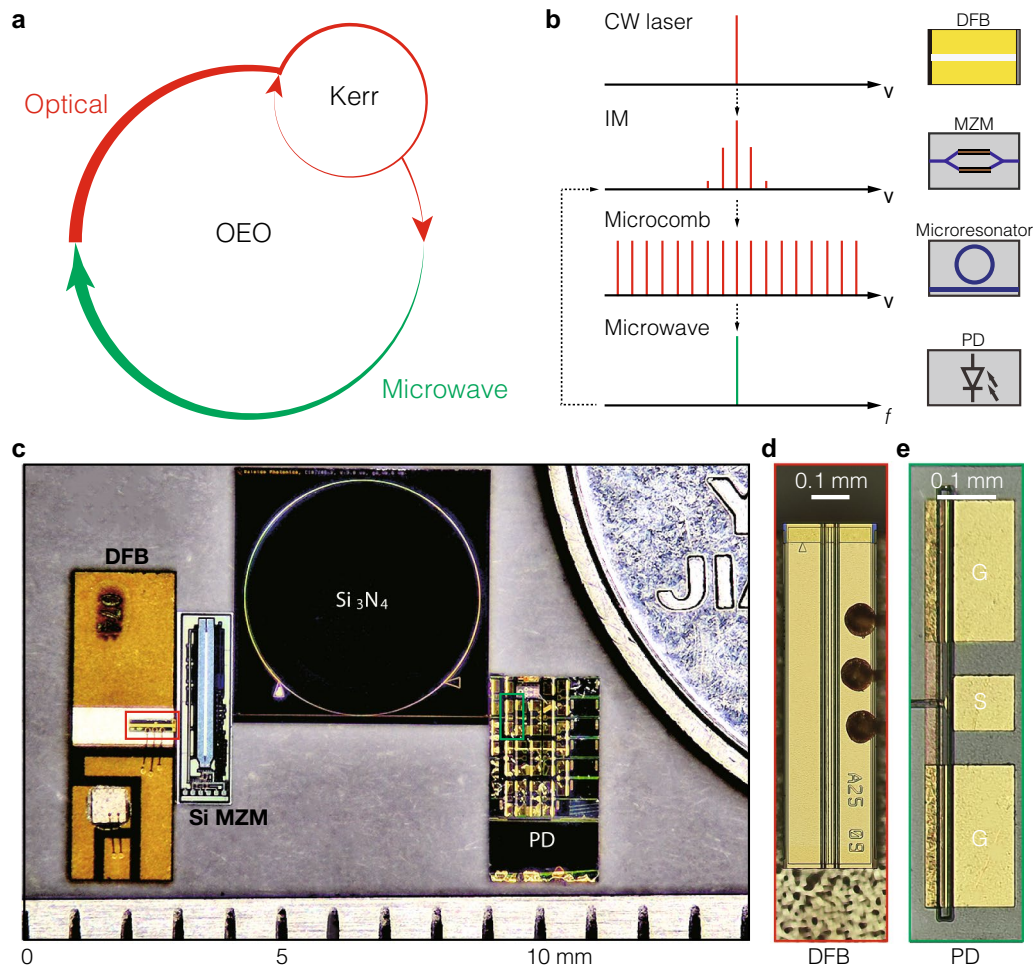
Fig. 1 Concept, principle and components of the optoelectronic-oscillator microcomb. **a**. Conceptual diagram of the self-starting and self-maintaining OEO microcomb via the feedback interplay of Kerr nonlinearity and optical-microwave conversion. **b**. Principle of the OEO microcomb. The DFB laser's CW output is intensity-modulated (IM) by an MZM. The CW pump and modulated sidebands are coupled into a high-Q optical microresonator. If the IM frequency f_{IM} matches the microresonator FSR, i.e. $f_{IM} = D_1/2\pi$, a coherent microcomb forms, whose line spacing is $f_{rep} = D_1/2\pi$. Detection of the microcomb's f_{rep} via a PD outputs a microwave of carrier frequency f_{rep}, which is injected to the MZM. As such, $f_{IM} = f_{rep} = D_1/2\pi$ is ensured. Consequently, the entire system can self-oscillate and self-maintain, harmonizing a coherent microcomb and a low-noise microwave. **c**. Photograph showing the four critical chip components of our OEO microcomb, i.e. the DFB laser chip, the Si MZM chip, the Si$_3$N$_4$ microresonator chip, and the PD chip, which are referenced to a ruler and compared with the size of a 1-Chinese-Jiao coin. The actual experimental setup including other optical and electronic components is shown in Fig. 3a. **d**. Optical microscope image of the DFB laser. **e**. Optical microscope image of the PD with GSG pads

our DFB laser does not allow for modulation speed above 1 GHz. Therefore, the Si MZM is required here.

Microresonator. The Si$_3$N$_4$ microresonator is fabricated using a foundry-level, deep-ultraviolet subtractive process with 300-nm-thick Si$_3$N$_4$ on 150-mm-diameter (6-inch) wafers [52, 53]. Light is coupled into and out of the Si$_3$N$_4$ microresonator's fundamental TE mode via inverse tapers at chip facets and a bus waveguide. At 1558 nm pump wavelength, the Si$_3$N$_4$ microresonator features $D_1/2\pi = 10.699$ GHz FSR. The microresonator's Q factor is evaluated by resonance fit

[54]. Figure 2e presents a typical resonance with fitted intrinsic loss $\kappa_0/2\pi = 8.6$ MHz, external coupling strength $\kappa_{ex}/2\pi = 5.7$ MHz, and loaded linewidth $\kappa/2\pi = (\kappa_0 + \kappa_{ex})/2\pi = 14.3$ MHz. The intrinsic quality factor is calculated as $Q_0 = \omega/\kappa_0$, where $\omega/2\pi$ is the resonant frequency. Figure 2f shows the histogram of 1,719 measured Q_0 values, with the most probable value $Q_0 = 21 \times 10^6$. As the 300 nm Si$_3$N$_4$ thickness endows the microresonator with normal group velocity dispersion (GVD, $D_2 < 0$), the generated microcomb is a dark pulse (platicon) stream in the time domain [22–26]. The
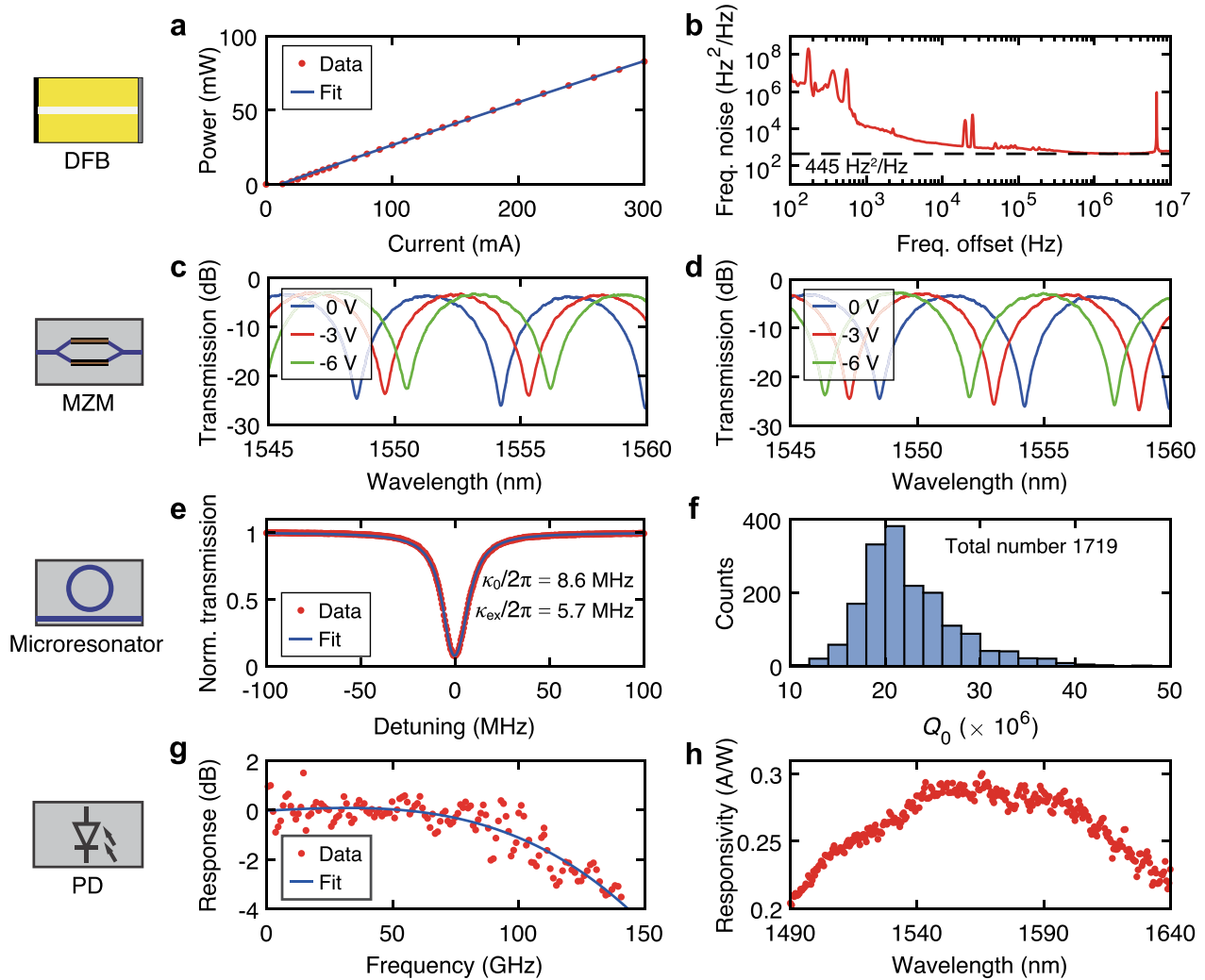
Fig. 2 Characterization of chips. **a**, **b**. Measured output optical power versus laser current (a), and single-sideband frequency noise PSD (b) of the free-running DFB laser. The 445 Hz^2/Hz white noise corresponds to 2.79 kHz intrinsic linewidth. **c**, **d**. Measured transmission spectra of the Si MZM with different bias voltage V_{dc} applied on the upper (c) or lower waveguide arm (d). **e**, **f**. A typical resonance of the Si$_3$N$_4$ microresonator with fitted $\kappa_0/2\pi = 8.6$ MHz and $\kappa_{ex}/2\pi = 5.7$ MHz (e), and the histogram of 1,719 measured Q_0 values with the most probable value $Q_0 = 21 \times 10^6$ (f). **g**, **h**. Measured detection bandwidth (g) and responsivity versus wavelength (h) of the PD chip. The 3-dB bandwidth is estimated over 120 GHz from the fitting

fabrication process flow and more characterization data of the Si$_3$N$_4$ microresonator are found in Supplementary Materials Note 3.

Photodetector. The PD chip has $3 \times 15\ \mu m^2$ active area, whose epitaxial structure is grown on a semi-insulating indium phosphide (InP) substrate [53, 55]. It collects incident light via a waveguide and outputs electrical signals via a ground-signal-ground (GSG) probe. Figure 2g shows the measured 3-dB bandwidth over 120 GHz. Such a broad bandwidth of the PD is not necessary for the microresonator with only 10.7 GHz FSR, but is required for high-repetition-rate microcomb generation in future experiments. Figure 2h shows that, within the detection

wavelength range of 1490 to 1640 nm, the measured responsivity is above 0.2 A/W and up to 0.3 A/W (reproduced from Ref. [53]). The fabrication process flow and more characterization data of the PD chip are found in Supplementary Materials Note 4.

2.2 Experimental setup

Figure 3a shows the experimental setup including optical and electronic components that are not integrated, in addition to the four types of chips described above. The DFB laser's CW output at 1558 nm wavelength is sent into the Si MZM. The intensity-modulated light from the Si MZM is power-boosted via an optical amplifier (OA),
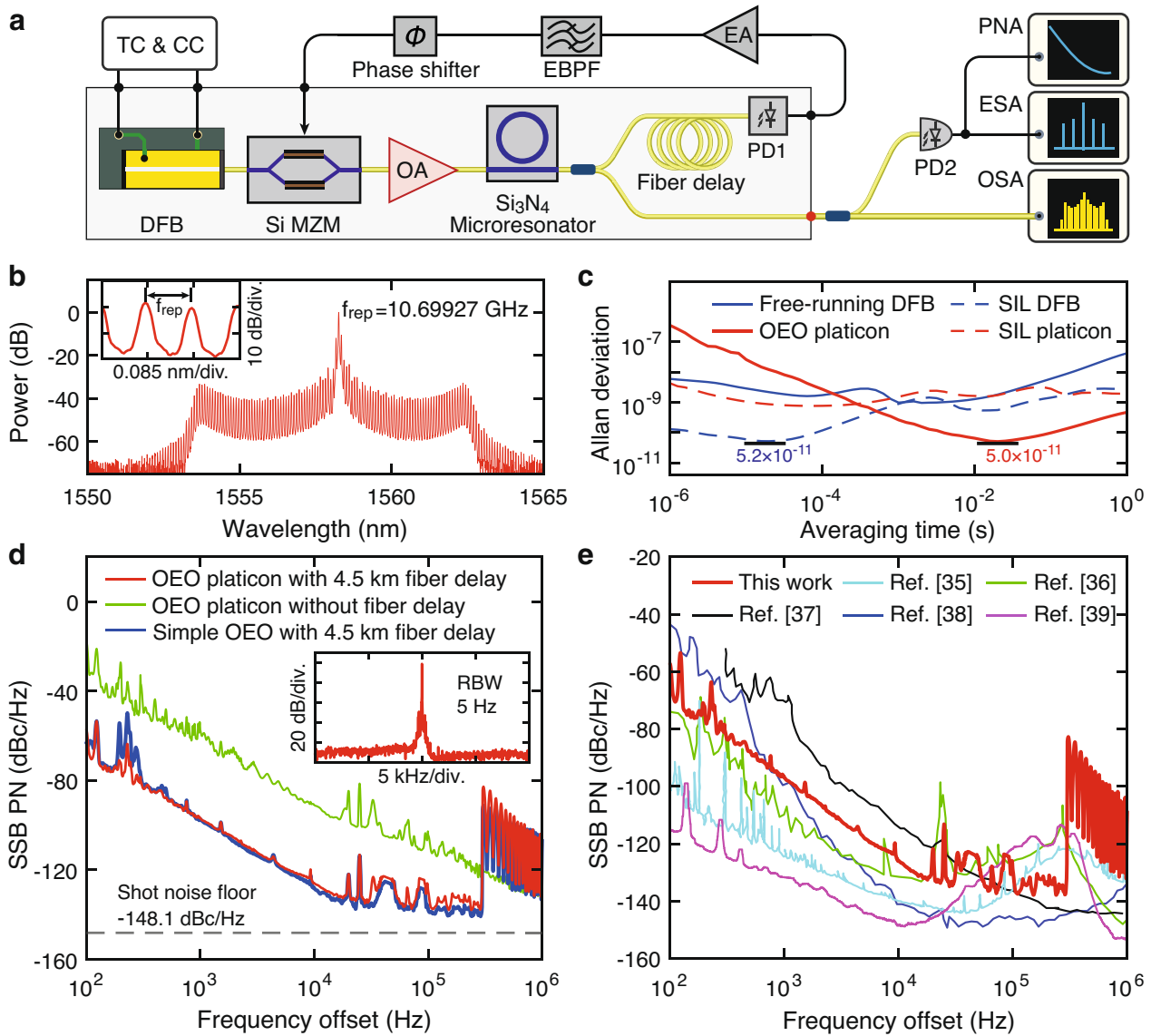
Fig. 3 Experimental setup and results of the optoelectronic-oscillator microcomb. **a.** Experimental setup. TC & CC, temperature control and current control. ESA, electrical spectrum analyzer. OSA, optical spectrum analyzer. PD1, the PD chip. PD2, the Finisar PD. **b.** Optical spectrum of the platicon microcomb. Inset shows 10.69927 GHz line spacing. **c.** Allan deviation data of the free-running DFB laser's frequency (optical, blue solid curve), and the OEO platicon's f_{rep} (microwave, red solid curve), in comparison with the SIL DFB laser's frequency (optical, blue dashed curve), and the SIL platicon's f_{rep} (microwave, red dashed curve) described in Ref. [53]. **d.** Phase noise data of the f_{rep} = 10.69927 GHz microwaves of the OEO platicon with (red curve) and without (green curve) 4.5 km fiber delay, in comparison with the conventional OEO with 4.5 km fiber delay (blue curve) and the estimated shot noise floor (dashed gray line). Inset shows the RF spectrum of the platicon microcomb's f_{rep}. RBW, resolution bandwidth. **e.** Phase noise data of our OEO platicon microcomb's f_{rep} = 10.69927 GHz (red curve), in comparison with the phase noise data using microcomb-based OFD (scaled to 10 GHz) in Ref. [35] (cyan curve), Ref. [36] (green curve), Ref. [37] (black curve), Ref. [38] (blue curve), Ref. [39] (magenta curve)

which in our case is an EDFA. The amplified light is then coupled into the Si_3N_4 microresonator and generates a platicon microcomb. Before detection with the high-speed PD chip (PD1), the platicon pulse stream travels through a 4.5-km-long single-mode fiber (SMF) whose function will be discussed later. The PD chip outputs a

microwave signal whose carrier frequency corresponds to the platicon's repetition rate f_{rep}. The microwave signal is power-boosted by an electronic amplifier (EA) and filtered by an electronic band-pass filter (EBPF). The EBPF's center frequency is fixed at $f_{rep} = D_1/2\pi = 10.699$ GHz and 3-dB bandwidth is 10 MHz. A phase shifter is used to

vary the phase of the feedback microwave signal before injecting the signal to drive the Si MZM.

With optimized combination of the DFB laser frequency, the EA gain, and the feedback microwave phase, a platicon microcomb and a low-noise microwave can synergistically self-start from the noise in the OEO loop and self-maintain. This is because the OEO satisfies the classical Barkhausen oscillation criteria of feedback-loop systems [43]. Because of the 4.5-km-long fiber delay, the OEO function endows the microwave with high spectral purity (i.e. low phase noise), which further purifies the modulation signal for the CW pump and improves the platicon's coherence.

Experimentally, the EA contains a two-stage low-noise amplifier (maximum 46 dB gain) and a voltage-variable attenuator (VVA, maximum 50 dB attenuation). The phase shifter is voltage-controlled, allowing for 0° to 360° loop phase variation. We treat 0° relative phase with 0 V applied. When the EA gain is set to 36 dB and the loop phase is 240°, the system self-oscillates. The optical spectrum of the platicon microcomb is shown in Fig. 3b. The inset highlights comb lines with 10.69927 GHz spacing. The ultimate microwave power applied on the Si MZM is measured as 19 dBm. We observe that the platicon microcomb can self-maintain with microwave power ranging from 16 to 22 dBm by varying the EA gain.

Previously, platicon microcombs in optical microresonators can be deterministically seeded by phase- or intensity-modulation of the CW pump [49, 50]. These methods necessitate an external microwave source operating at a high frequency to match the microresonator FSR, which is bulky, power-hungry and expensive. Here we obviate external microwave sources by utilizing the microwave synthesized via photodetection of the platicon's f_{rep} and the OEO loop. In addition, the microwave frequency is selected by the EBPF – a passive component that is simple, small, stable and does not consume power.

2.3 Coherence optimization
The mutual coherence of the platicon's comb lines is characterized by photodetection of the platicon's f_{rep} using another PD (PD2, Finisar XPDV3120R-VF-FA) and analysis of single-sideband RF phase noise (SSB RF PN) of f_{rep} using a phase noise analyzer (PNA). Figure 3d green curve shows the measured microwave phase noise of the OEO platicon's f_{rep} without fiber delay, which reaches $-57/-91/-104$ dBc/Hz at 1/10/100 kHz Fourier frequency offset. To purify the microwave, a 4.5-km-long fiber delay is introduced, as exemplified in Ref. [45]. Typically, a longer fiber leads to lower microwave phase noise. However, there are parasitic limitations on the allowed maximum fiber length. First, a longer fiber results in smaller OEO mode spacing. In our case with

4.5 km fiber length, the mode spacing is 43.6 kHz. Second, the side-mode suppression ratio (SMSR) decreases as the fiber length increases. For example, the SMSR is around 35(50) dB for 4.5(2.0) km fiber length. These two effects together cause multi-mode competition, resulting in instability, mode-hopping and extra noise. The EBPF of 10 MHz bandwidth ameliorates this issue and allows for stable oscillation with 4.5 km fiber length. Meanwhile, the 10 MHz bandwidth is also sufficiently large to facilitate alignment of the OEO frequency and the Si_3N_4 microresonator FSR. Measured OEO microwave's phase noise with different fiber delay length is compared in Supplementary Materials Note 5. Practically, the SMSR can be improved by a multi-loop OEO structure [56].

Finally, with 4.5 km fiber delay, the phase noise of our OEO platicon's f_{rep} reaches $-97/-126/-130$ dBc/Hz at 1/10/100 kHz Fourier frequency offset, as shown in Fig. 3d red curve. The inset shows the electrical power spectrum of the f_{rep} = 10.69927 GHz microwave with 5 Hz resolution bandwidth. In comparison, we also measure the conventional OEO microwave's phase noise without platicon formation and with 4.5 km fiber delay, as shown in Fig. 3d blue curve. The microwave phase noises with and without platicon formation are nearly identical, indicating that f_{rep} directly inherits coherence from the OEO microwave. Thus we have not observed the microcomb-induced spectral purification effects described in Ref. [19, 27, 50]. The reason is due to the fact that our microwave phase noise is already sufficiently low. More experimental data to quantify the spectral purification effect are found in Supplementary Materials Note 6.

Figure 3c shows the measured Allan deviation data of the free-running DFB laser's frequency (optical, blue solid curve), and the OEO platicon's f_{rep} (microwave, red solid curve), using the PNA. In comparison, the Allan deviation data of the self-injection-locked (SIL) DFB laser's frequency (optical, blue dashed curve), and the SIL platicon's f_{rep} (microwave, red dashed curve), from Ref. [53], are shown. It is evident that the frequency instability of the OEO platicon's f_{rep} is significantly lower than that of the SIL platicon's f_{rep}, though the free-running DFB laser is less stable than the SIL DFB laser. The long-term drift (> 10 ms) of our OEO platicon's f_{rep} is mainly determined by the DFB laser's frequency drift and the thermal drift of the long fiber delay.

The phase noise of f_{rep} increases from -126 dBc/Hz to -118 dBc/Hz at 10 kHz offset by varying the EA gain. A large gain can introduce bumps on the phase noise curve as detailed in Supplementary Materials Note 7. Reference [43] illustrates the influence of loop gain on the bifurcation sequence in the OEO. There is an optimum loop gain range such that Hopf bifurcation with constant amplitude generates an ultra-pure microwave.

Such an optimum gain is also found in our experiment. Meanwhile, Supplementary Materials Note 8 investigates possible reasons that limit our microwave phase noise. For example, phase noise can be further reduced to $-102/-130/-131$ dBc/Hz at 1/10/100 kHz offset by replacing the chip PD with a commercial PD (another Finisar XPDV3120R-VF-FA). Meanwhile, replacing the Si MZM with a commercial lithium niobate electro-optic modulator (LiNbO$_3$ EOM, iXblue MXAN-LN-10-PD) reduces phase noise at low Fourier frequency offset, e.g. 14(5) dB reduction at 0.1(1) kHz offset. The reasons are likely due to the fact that both the Si MZM and the chip PD are not fully packaged, where optical and microwave power fluctuation induced by mechanical vibration on these devices causes loop gain jittering. In addition, we do not observe phase noise reduction by replacing the DFB laser with an external-cavity diode laser (ECDL, Toptica CTL).

Figure 3e compares our 10.69927 GHz microwave's phase noise with scaled 10 GHz microwave's phase noise from recent microcomb-based OFD works [35–39]. Different from Ref. [35–39], our OEO-platicon-based microwave generation does not require any active locking, servos, multiple lasers, and external RF or microwave sources for reference or regulation. Note that our

microwave's phase noise below 1 kHz offset remains relatively high. Possible reasons causing this issue are discussed in Supplementary Materials Note 5.

3 Discussion

Towards heterogeneous integration. While the DFB laser, the Si MZM, the Si$_3$N$_4$ microresonator, and the PD are photonic chips, the entire OEO platicon system is not yet fully integrated. Nevertheless, with maturing heterogeneous integration and photonic-electronic co-packaging, our OEO microcomb system has the potential to be fully integrated [57]. Figure 4 depicts an envisaged fully integrated architecture. The photonic Damascene process [58] is advantageous to fabricate ultralow-loss Si$_3$N$_4$ waveguides and microresonators with a planarized top surface, ideal for wafer bonding of other thin films [12, 59] and micro-transfer printing [60]. On Si$_3$N$_4$ waveguides, DFB lasers and PDs can be heterogeneously integrated, as described in Ref. [12] and Ref. [61], respectively. In addition to Si MZMs that are naturally compatible with heterogeneous integration on Si$_3$N$_4$, thin-film LiNbO$_3$ EOMs can also be integrated on Si$_3$N$_4$ as demonstrated in Ref. [62]. In particular, broadband LiNbO$_3$ EOMs allow OEO microcomb generation with repetition rate over 100 GHz, critical for applications in
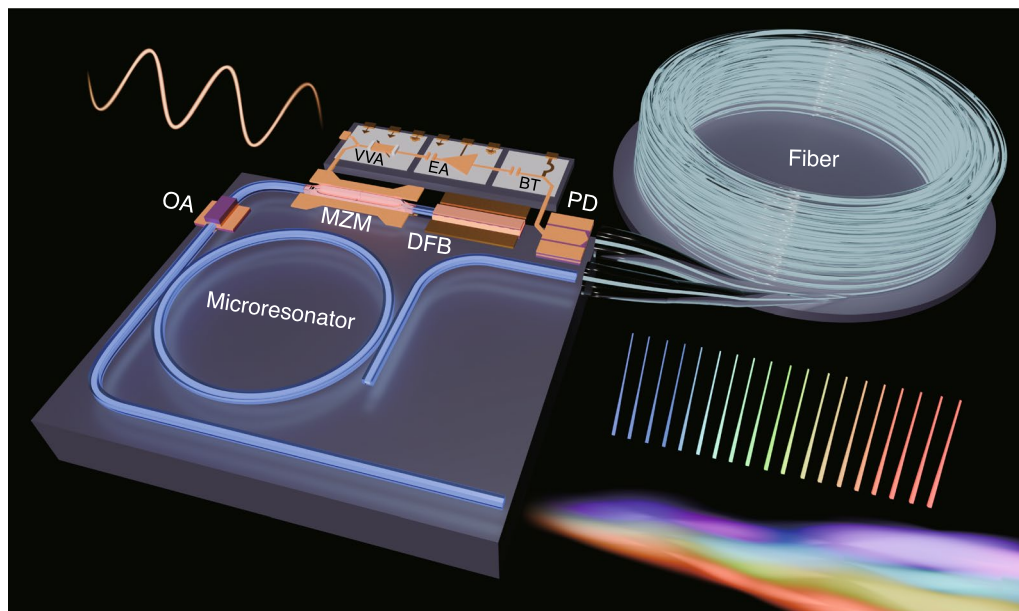

Fig. 4 Envisaged architecture of a fully integrated OEO microcomb. The CW light emitted from a DFB laser is intensity-modulated by a high-speed MZM. The modulated CW laser is power-amplified, and then couples into a Kerr microresonator via the through port. The output light from the microresonator's drop port is injected into a tightly winded fiber. The output light from the fiber is detected by a PD. The converted electrical signal goes through a series of microelectronic elements, comprising a bias tee (BT), an electrical amplifier (EA), and a voltage-variable attenuator (VVA). The signal from the VVA is fed back to drive the MZM. The generated microcomb is collected from the output of the microresonator's through port. Note that, only when the CW carrier and the intensity-modulation sidebands are aligned with the microresonator resonances, they are allowed to exit from the microresonator via the drop port. Thus, the microresonator with the drop and through ports functions as a narrowband RF mode selector, which only selects the OEO frequency corresponding to the microresonator's FSR

coherent communication and ranging [63]. The optical amplifier can be erbium-doped Si_3N_4 waveguides [64] or III-V semiconductor optical amplifiers [65]. Meanwhile, ultralow-loss waveguides and microresonators can also be made of $LiNbO_3$ [66, 67], allowing microwave-rate bright soliton [68] or dark pulse [69] generation. In such a way, the inclusion of EOMs is straightforward [70, 71] and does not require heterogeneous integration. Lasers and PDs can be heterogeneously integrated on $LiNbO_3$ [72]. The optical amplifier can be erbium-doped $LiNbO_3$ waveguides [73] or III-V semiconductor optical amplifiers [74].

As it is impossible to fabricate kilometer-long integrated waveguides, fiber can only be hybrid-integrated or packaged to the OEO microcomb chip, as well as the microelectronic chip containing the VVA, EA and bias-tee. In our experiment, the tightly winded fiber has a volume below 500 cm^3. The RF phase shifter in Fig. 3a can also be omitted with the long fiber, as discussed in Supplementary Materials Note 9. In addition, Fig. 4 shows that the microresonator with a drop port can serve as an optical band-pass filter in the OEO. The pump carrier and the sidebands are allowed to pass through the microresonator only if they all align with the microresonator's resonances, resulting in narrowband selection of the OEO mode at the microresonator FSR. Meanwhile, amplified spontaneous emission (ASE) noise from the optical amplifier is suppressed. In such a way, the EBPF can be excluded and the required fiber length can be significantly shortened with the high-Q microresonator [71]. This leads to not only reduced size and weight, but also a more stable microcomb with relaxed OEO multi-mode competition.

Conclusion. In conclusion, we have demonstrated an OEO microcomb that spontaneously harmonizes a coherent microcomb and a low-noise microwave. The critical components of our OEO microcomb involve a high-power DFB laser, a broadband Si MZM, an ultralow-loss Si_3N_4 microresonator, and a high-speed PD. Each component represents the state of the art in its own class, yet can be manufactured in large volume with low cost and high yield using established CMOS and III-V foundries. The synthesized microcomb features 10.7 GHz repetition rate with phase noise of $-97/-126/-130$ dBc/Hz at 1/10/100 kHz Fourier frequency offset. Compared to our previous demonstration of fully integrated microcomb-based microwave oscillators [53], our current OEO microcomb – also entirely passive but not yet fully integrated – allows further noise reduction especially at the low Fourier frequency offset, i.e. 12/22/21 dB reduction at 0.1/1/10 kHz offset. This critical improvement is attributed to the introduction of the OEO feedback loop, which is simple yet endows major spectral

purity. This microwave phase noise of our OEO microcomb is on par with state-of-the-art integrated OEOs, as compared in Supplementary Materials Note 10. In contrast to recent demonstrations using microcomb-based OFD [35–39], our OEO microcomb can achieve comparable phase noise performance [37, 38] by inheriting the OEO microwave's coherence. Yet it is entirely passive, and does not require extensive active locking, additional lasers, and external RF or microwave sources, as well as sophisticated initiation. Besides, we find that the previously observed microcomb-induced spectral purification effects [19, 27, 50] are absent in our OEO microcomb, and conclude that the generated microcomb does not reciprocally purify the microwave regulating the microcomb. Our work paves a greatly simplified route to symphonizing coherent and robust microcombs and microwaves. Moreover, with the fast evolving heterogeneous and hybrid integration, our OEO microcomb has promising potential to be fully integrated on a monolithic chip with improved stability. Our OEO microcomb can become an invaluable technology and building block for microwave photonics, radio-over-fiber, and optical communication.

Supplementary Information

The online version contains supplementary material available at https://doi.org/10.1186/s43593-025-00094-w.

Supplementary file 1.

Author contributions

J. Long, Z. W., W. S. and J. H. built the experimental setup. Z. W., J. Long, H. P. and W. S. performed the experiments and analyzed the data, with the assistance from D. C., Y.-H. L. and J. H.. L. G., B. S. and C. S. fabricated and characterized the Si_3N_4 chip. Shuyi L. and Z. L. fabricated and characterized the Si MZM chip. L. L, T. L. and B. C. fabricated and characterized the PD chip. J. Long, W. S. and Shichang L. characterized and packaged the DFB lasers. J. Long, Z. W., W. S., H. P. and J. Liu wrote the manuscript, with the input from others. J. Liu supervised the project.

Declarations

References

1. T. Udem, R. Holzwarth, T.W. Hänsch, Optical frequency metrology. Nature **416**, 233–237 (2002). https://doi.org/10.1038/416233a
2. S.T. Cundiff, J. Ye, Colloquium: femtosecond optical frequency combs. Rev. Mod. Phys. **75**, 325–342 (2003). https://doi.org/10.1103/RevModPhys.75.325
3. T. Fortier, E. Baumann, 20 years of developments in optical frequency comb technology and applications. Commun. Phys. **2**, 153 (2019). https://doi.org/10.1038/s42005-019-0249-y
4. T.J. Kippenberg, A.L. Gaeta, M. Lipson, M.L. Gorodetsky, Dissipative Kerr solitons in optical microresonators. Science **361**, eaan8083 (2018). https://doi.org/10.1126/science.aan8083
5. A.L. Gaeta, M. Lipson, T.J. Kippenberg, Photonic-chip-based frequency combs. Nat. Photonics **13**, 158–169 (2019). https://doi.org/10.1038/s41566-019-0358-x
6. S.A. Diddams, K. Vahala, T. Udem, Optical frequency combs: Coherently uniting the electromagnetic spectrum. Science **369**, eaay3676 (2020). https://doi.org/10.1126/science.aay3676
7. D.J. Moss, R. Morandotti, A.L. Gaeta, M. Lipson, New CMOS-compatible platforms based on silicon nitride and hydex for nonlinear optics. Nat. Photonics **7**, 597–607 (2013). https://doi.org/10.1038/nphoton.2013.183
8. A. Kovach et al., Emerging material systems for integrated optical Kerr frequency combs. Adv. Opt. Photon. **12**, 135–222 (2020). https://doi.org/10.1364/AOP.376924
9. A. Dutt, A. Mohanty, A.L. Gaeta, M. Lipson, Nonlinear and quantum photonics using integrated optical materials. Nat. Rev. Mater. **9**, 321–346 (2024). https://doi.org/10.1038/s41578-024-00668-z
10. T. Komljenovic et al., Heterogeneous silicon photonic integrated circuits. J. Lightwave Technol. **34**, 20–35 (2016). https://doi.org/10.1109/JLT.2015.2465382
11. B. Stern, X. Ji, Y. Okawachi, A.L. Gaeta, M. Lipson, Battery-operated integrated frequency comb generator. Nature **562**, 401–405 (2018). https://doi.org/10.1038/s41586-018-0598-9
12. C. Xiang et al., Laser soliton microcombs heterogeneously integrated on silicon. Science **373**, 99–103 (2021). https://doi.org/10.1126/science.abh2076
13. P. Del'Haye et al., Optical frequency comb generation from a monolithic microresonator. Nature **450**, 1214–1217 (2007). https://doi.org/10.1038/nature06401
14. T. Herr et al., Temporal solitons in optical microresonators. Nat. Photonics **8**, 145–152 (2014). https://doi.org/10.1038/nphoton.2013.343
15. V. Brasch et al., Photonic chip-based optical frequency comb using soliton Cherenkov radiation. Science **351**, 357–360 (2016). https://doi.org/10.1126/science.aad4811
16. C. Joshi et al., Thermally controlled comb generation and soliton mode-locking in microresonators. Opt. Lett. **41**, 2565–2568 (2016). https://doi.org/10.1364/OL.41.002565
17. W. Liang et al., High spectral purity Kerr frequency comb radio frequency photonic oscillator. Nat. Commun. **6**, 7957 (2015). https://doi.org/10.1038/ncomms8957
18. X. Yi, Q.-F. Yang, K.Y. Yang, M.-G. Suh, K. Vahala, Soliton frequency comb at microwave rates in a high-Q silica microresonator. Optica **2**, 1078–1085 (2015). https://doi.org/10.1364/OPTICA.2.001078
19. J. Liu et al., Photonic microwave generation in the X- and K-band using integrated soliton microcombs. Nat. Photonics **14**, 486–491 (2020). https://doi.org/10.1038/s41566-020-0617-x
20. S. Zhang et al., Terahertz wave generation using a soliton microcomb. Opt. Express **27**, 35257–35266 (2019). https://doi.org/10.1364/OE.27.035257
21. T. Tetsumoto et al., Optically referenced 300 GHz millimetre-wave oscillator. Nat. Photonics **15**, 516–522 (2021). https://doi.org/10.1038/s41566-021-00790-2
22. X. Xue et al., Mode-locked dark pulse Kerr combs in normal-dispersion microresonators. Nat. Photonics **9**, 594–600 (2015). https://doi.org/10.1038/nphoton.2015.137
23. V.E. Lobanov, G. Lihachev, T.J. Kippenberg, M.L. Gorodetsky, Frequency combs and platicons in optical microresonators with normal GVD. Opt. Express **23**, 7713–7721 (2015). https://doi.org/10.1364/OE.23.007713
24. S.-W. Huang et al., Mode-locked ultrashort pulse generation from on-chip normal dispersion microresonators. Phys. Rev. Lett. **114**, 053901 (2015). https://doi.org/10.1103/PhysRevLett.114.053901
25. P. Parra-Rivas, D. Gomila, E. Knobloch, S. Coen, L. Gelens, Origin and stability of dark pulse Kerr combs in normal dispersion resonators. Opt. Lett. **41**, 2402–2405 (2016). https://doi.org/10.1364/OL.41.002402
26. E. Nazemosadat et al., Switching dynamics of dark-pulse Kerr frequency comb states in optical microresonators. Phys. Rev. A **103**, 013513 (2021). https://doi.org/10.1103/PhysRevA.103.013513
27. W. Weng et al., Spectral purification of microwave signals with disciplined dissipative Kerr solitons. Phys. Rev. Lett. **122**, 013902 (2019). https://doi.org/10.1103/PhysRevLett.122.013902
28. R. Liu et al., Low-phase-noise microwave generation with a free-running dual-pumped Si_3N_4 soliton microcomb. Opt. Lett. **49**, 754–757 (2024). https://doi.org/10.1364/OL.511039
29. E. Lucas et al., Ultralow-noise photonic microwave synthesis using a soliton microcomb-based transfer oscillator. Nat. Commun. **11**, 374 (2020). https://doi.org/10.1038/s41467-019-14059-4
30. X. Yi et al., Single-mode dispersive waves and soliton microcomb dynamics. Nat. Commun. **8**, 14869 (2017). https://doi.org/10.1038/ncomms14869
31. Q.-F. Yang et al., Dispersive-wave induced noise limits in miniature soliton microwave sources. Nat. Commun. **12**, 1442 (2021). https://doi.org/10.1038/s41467-021-21658-7
32. T.M. Fortier et al., Generation of ultrastable microwaves via optical frequency division. Nat. Photonics **5**, 425–429 (2011). https://doi.org/10.1038/nphoton.2011.121
33. X. Xie et al., Photonic microwave signals with zeptosecond-level absolute timing noise. Nat. Photonics **11**, 44–47 (2017). https://doi.org/10.1038/nphoton.2016.215
34. J. Li, X. Yi, H. Lee, S.A. Diddams, K.J. Vahala, Electro-optical frequency division and stable microwave synthesis. Science **345**, 309–313 (2014). https://doi.org/10.1126/science.1252909
35. I. Kudelin et al., Photonic chip-based low-noise microwave oscillator. Nature **627**, 534–539 (2024). https://doi.org/10.1038/s41586-024-07058-z
36. S. Sun et al., Integrated optical frequency division for microwave and mmWave generation. Nature **627**, 540–545 (2024). https://doi.org/10.1038/s41586-024-07057-0
37. Y. Zhao et al., All-optical frequency division on-chip using a single laser. Nature **627**, 546–552 (2024). https://doi.org/10.1038/s41586-024-07136-2
38. Y. He et al., Chip-scale high-performance photonic microwave oscillator. Sci. Adv. **10**, eado9570 (2024). https://doi.org/10.1126/sciadv.ado9570
39. X. Jin et al., Microresonator-referenced soliton microcombs with zeptosecond-level timing noise. Nat. Photonics **19**, 630–636 (2025). https://doi.org/10.1038/s41566-025-01669-2
40. L. Maleki, The optoelectronic oscillator. Nat. Photonics **5**, 728–730 (2011). https://doi.org/10.1038/nphoton.2011.293
41. J. Tang et al., Integrated optoelectronic oscillator. Opt. Express **26**, 12257–12265 (2018). https://doi.org/10.1364/OE.26.012257
42. H. Peng, P. Lei, X. Xie, Z. Chen, Dynamics and timing-jitter of regenerative RF feedback assisted resonant electro-optic frequency comb. Opt. Express **29**, 42435–42456 (2021). https://doi.org/10.1364/OE.440621
43. Y.K. Chembo, D. Brunner, M. Jacquot, L. Larger, Optoelectronic oscillators with time-delayed feedback. Rev. Mod. Phys. **91**, 035006 (2019). https://doi.org/10.1103/RevModPhys.91.035006
44. T. Hao et al., Recent advances in optoelectronic oscillators. Adv. Photon. **2**, 044001 (2020). https://doi.org/10.1117/1.AP.2.4.044001
45. D. Eliyahu, D. Seidel & L. Maleki, Phase noise of a high performance OEO and an ultra low noise floor cross-correlation microwave photonic

homodyne system. 2008 IEEE International Frequency Control Symposium. 811–814 (2008). https://doi.org/10.1109/FREQ.2008.4623111.

46. T. Hao, W. Li, N. Zhu, M. Li, Perspectives on optoelectronic oscillators. APL Photonics **8**, 020901 (2023). https://doi.org/10.1063/5.0134289

47. D.C. Cole et al., Kerr-microresonator solitons from a chirped background. Optica **5**, 1304–1310 (2018). https://doi.org/10.1364/OPTICA.5.001304

48. R. Miao et al., Repetition rate locked single-soliton microcomb generation via rapid frequency sweep and sideband thermal compensation. Photon. Res. **10**, 1859–1867 (2022). https://doi.org/10.1364/PRJ.458472

49. V.E. Lobanov, N.M. Kondratiev, A.E. Shitikov, R.R. Galiev, I.A. Bilenko, Generation and dynamics of solitonic pulses due to pump amplitude modulation at normal group-velocity dispersion. Phys. Rev. A **100**, 013807 (2019). https://doi.org/10.1103/PhysRevA.100.013807

50. H. Liu et al., Stimulated generation of deterministic platicon frequency microcombs. Photon. Res. **10**, 1877–1885 (2022). https://doi.org/10.1364/PRJ.459403

51. S. Li, W. Luo, Z. Li, J. Liu, High-speed Mach-Zehnder modulators based on nonlinear optics and complex band structures. Phys. Rev. Applied **24**, 014021 (2025). https://doi.org/10.1103/f5v4-n5dw

52. Z. Ye et al., Foundry manufacturing of tight-confinement, dispersion-engineered, ultralow-loss silicon nitride photonic integrated circuits. Photon. Res. **11**, 558–568 (2023). https://doi.org/10.1364/PRJ.486379

53. W. Sun et al., A chip-integrated comb-based microwave oscillator. Light Sci. Appl. **14**, 179 (2025). https://doi.org/10.1038/s41377-025-01795-0

54. Y.-H. Luo et al., A wideband, high-resolution vector spectrum analyzer for integrated photonics. Light Sci. Appl. **13**, 83 (2024). https://doi.org/10.1038/s41377-024-01435-z

55. L. Li, L. Wang, B. Chen, High-speed waveguide modified uni-traveling carrier photodiodes with 130 GHz bandwidth. In 2023 Opto-Electronics and Communications Conference (OECC). 1–3 (2023). https://doi.org/10.1109/OECC56963.2023.10209607

56. X. Yao, L. Maleki, Multiloop optoelectronic oscillator. IEEE J. Quantum Electron. **36**, 79–84 (2000). https://doi.org/10.1109/3.817641

57. C. Xiang, J.E. Bowers, Building 3D integrated circuits with electronics and photonics. Nat. Electron. **7**, 422–424 (2024). https://doi.org/10.1038/s41928-024-01187-z

58. J. Liu et al., High-yield, wafer-scale fabrication of ultralow-loss, dispersion-engineered silicon nitride photonic circuits. Nat. Commun. **12**, 2236 (2021). https://doi.org/10.1038/s41467-021-21973-z

59. L. Chang et al., Heterogeneous integration of lithium niobate and silicon nitride waveguides for wafer-scale photonic integrated circuits on silicon. Opt. Lett. **42**, 803–806 (2017). https://doi.org/10.1364/OL.42.000803

60. G. Roelkens et al., Present and future of micro-transfer printing for heterogeneous photonic integrated circuits. APL Photonics **9**, 010901 (2024). https://doi.org/10.1063/5.0181099

61. Q. Yu et al., Heterogeneous photodiodes on silicon nitride waveguides. Opt. Express **28**, 14824–14830 (2020). https://doi.org/10.1364/OE.387939

62. M. Churaev et al., A heterogeneously integrated lithium niobate-on-silicon nitride photonic platform. Nat. Commun. **14**, 3499 (2023). https://doi.org/10.1038/s41467-023-39047-7

63. B.C. Yao et al., Interdisciplinary advances in microcombs: bridging physics and information technology. eLight **4**, 19 (2024). https://doi.org/10.1186/s43593-024-00071-9

64. Y. Liu et al., A photonic integrated circuit–based erbium-doped amplifier. Science **376**, 1309–1313 (2022). https://doi.org/10.1126/science.abo2631

65. C.O. de Beeck et al., Heterogeneous III-V on silicon nitride amplifiers and lasers via microtransfer printing. Optica **7**, 386–393 (2020). https://doi.org/10.1364/OPTICA.382989

66. D. Zhu et al., Integrated photonics on thin-film lithium niobate. Adv. Opt. Photon. **13**, 242–352 (2021). https://doi.org/10.1364/AOP.411024

67. M. Zhang. C. Wang, R. Cheng, A. Shams-Ansari, M. Lončar, Monolithic ultra-high-*Q* lithium niobate microring resonator. Optica **4**, 1536–1537 (2017). https://doi.org/10.1364/OPTICA.4.001536

68. Y. He et al., High-speed tunable microwave-rate soliton microcomb. Nat. Commun. **14**, 3467 (2023). https://doi.org/10.1038/s41467-023-39229-3

69. X. Lv et al., Broadband microwave-rate dark pulse microcombs in dissipation-engineered LiNbO$_3$ microresonators. Nat. Commun. **16**, 2389 (2025). https://doi.org/10.1038/s41467-025-57736-3

70. C. Wang et al., Integrated lithium niobate electro-optic modulators operating at CMOS-compatible voltages. Nature **562**, 101–104 (2018). https://doi.org/10.1038/s41586-018-0551-y

71. R. Ma et al., Ka-band thin film lithium niobate photonic integrated optoelectronic oscillator. Photon. Res. **12**, 1283–1293 (2024). https://doi.org/10.1364/PRJ.521301

72. M. Li et al., Heterogeneously-integrated self-injection locked lasers on thin film lithium niobate. In Optical Fiber Communications Conference(OFC). 1–3 (2024). https://doi.org/10.1364/OFC.2024.W1K.3

73. Z. Chen et al., Efficient erbium-doped thin-film lithium niobate waveguide amplifiers. Opt. Lett. **46**, 1161–1164 (2021). https://doi.org/10.1364/OL.420250

74. C.O. de Beeck et al., III/V-on-lithium niobate amplifiers and lasers. Optica **8**, 1288–1289 (2021). https://doi.org/10.1364/OPTICA.438620